International Journal for Multidisciplinary Research (IJFMR)

E-ISSN: 2582-2160 ● Website: www.ijfmr.com ● Email: editor@ijfmr.com

Numerical Analysis of MHD Flow and Heat Transfer of a Nanofluid over a Stretching Surface with Thermal Radiation

Dr K. K. Tiwari

Principal, Constituent Government College Richha, Baheri, Bareilly

Abstract:
This study investigates steady, two-dimensional magnetohydrodynamic (MHD) boundary-layer flow and heat transfer of an Al_2O_3–water nanofluid over a linearly stretching sheet in the presence of additive Rosseland thermal radiation. The similarity-reduced momentum and energy equations were solved with an adaptive collocation boundary-value method. Solver accuracy was verified against the exact Newtonian MHD stretching-sheet relation, with a maximum wall-shear error below 0.001%. Rather than relying on a few one-factor profile plots, the study evaluates the complete $5 \times 5 \times 5$ parameter grid: magnetic parameter M = 0–2, radiation parameter Rd = 0–2, and nanoparticle volume fraction φ = 0–0.04, yielding 125 deterministic computational runs. These runs are design points, not random experimental observations; therefore, correlations, regression coefficients, ANOVA quantities, and nominal p values are interpreted as design-space screening diagnostics rather than population-level inferential statistics. Across marginal means, increasing M from 0 to 2 increased reduced wall drag by 73.2% and decreased the reduced total Nusselt response by 13.7%. Increasing Rd from 0 to 2 increased the reduced total Nusselt response by 48.2%. Increasing φ from 0 to 0.04 increased marginal mean wall drag by 11.3% and the total Nusselt response by 1.5%. The radiation result is not contradictory: higher Rd thickens the thermal field and reduces the local dimensionless wall-temperature gradient, but the reported total Nusselt response multiplies the wall gradient by the combined conductive-plus-radiative conductivity contribution, which more than offsets that gradient reduction over the present design space. The first-order heat-transfer model gave $R^2 = 0.9705$, whereas the quadratic response-surface model achieved adjusted $R^2 = 0.9995$ and identified important $M \times Rd$, $M \times \varphi$, and $Rd \times \varphi$ interactions. The principal novelty is the integration of a benchmark-validated similarity solver, a complete factorial computational dataset, explicit heat-flux definition, and reproducible response-surface screening in a single framework for radiative MHD nanofluid analysis.

Keywords: Magnetohydrodynamics; Nanofluid; Stretching Surface; Thermal Radiation; Numerical Analysis; Response Surface.

1. Introduction

Flow over an ever-stretching surface is a canonical boundary-layer endeavor that has immediate application in polymer extrusion, wire drawing, glass-fiber production, continuous-casting, coating, metallurgical processing as well as thermal manufacturing. The boundary-layer structure of continuous moving faces was formulated by Sakiadis (1961a, 1961b) and Crane (1970), who got the same kind of exact similarity solution of a plate having linear extensions. The Simple extensions of the law of stretching included surface permeability and heat generation, but surface permeability was not studied until later (Magyari and Keller, 1999; Nandeppanavar et al., 2011), and fluid rheology, which is typically not largely about surface permeability, did so (Cortell, 2007, 2008a, 2008b, 2011). These papers firmed the stretching sheet as an effective physical model and a serious test-bed of nonlinear boundary-value solvers. With the introduction of fluids that are conducting on an electrical basis, there is a controllable magnetohydrodynamic process. A transverse magnetic field imposed creates a Lorentz force opposing streams flowing across the grain, which may change the momentum and thermal boundary-layer thickness, as well as modify the thermal boundary-layer thicknesses. When processing materials, this magnetic braking effect may be used to control the uniform flow of materials and heat removal without mechanical contact. MHD stretching-sheet applications thus grow more and more to include magnetic influences with porosity, suction or injection, slip, non-Newtonian constitutive laws, and convective boundary conditions (Hamad, 2011; Ibrahim and Shankar, 2013; Kandasamy et al., 2011; Mabood et al., 2015). One inescapable numerical finding is that, with the magnetic parameter held constant, the velocity field is suppressed and, in all cases where Joule heating, viscous dissipation, radiative cooling and temperature-dependent properties are maintained, the wall shear increases. The second pathway to therapy-based alteration to thermal transport is via nanofluids. The principle is based on dispensation of nanoscale solids with relatively high thermal conductivity, into a carrier liquid. Initial thermal-property experiments and simulations of enclosures had established that loading in a particle can alter the effective transport by a matter of scale and Buongiorno (2006) differentiated between Brownian diffusion and thermophoresis as significant in the dilute nanofluid convection. Subsequently, the two-component transport models or effective single-phase property models were introduced as the main components of the stretching-sheet models, and the influential boundary-layer models were given by Khan and Pop (2010), Makinde and Aziz (2011), Nadeem and Lee (2012), and Rana and Bhargava (2012). Hybrid nanofluids took the concept further and incorporated over one type of nanoparticles to fine-tune thermal and rheological functionality (Devi and Devi, 2016; Mahabaleshwar et al., 2021; Yashkun et al., 2020). In high temperature applications, thermally emitting media, high temperature paint, solar-thermal applications, furnace, and radiatively taking substances, thermal radiation is especially important at high temperature. When the radiative heat flux is shallow, the Rosseland diffusion approximation tends to replace the radiative heat flux by an effective diffusion term when the medium is optically thick, and make the radiative parameter in the energy equation. Radiative stretching flow studies have demonstrated that radiation alters the temperature distribution, and the rate of heat-transfer at the wall; but this is subject to the definition of the parameter. In a recipe where the radiation supplements effective thermal conductivity, intense radiation enhances the thickness of the thermal field and can possibly increase the cumulative wall heat exfiltration since radiation and conduction work concurrently (Hady et al., 2012; Rashidi et al., 2014; Sajid and Hayat, 2008; Shateyi and Prakash, 2014). Recent efforts also embrace the integration of radiation and hybrid nanofluids, micropolarity, chemical reaction, bioconvection, nonlinear stretching, and response modeling (Alrihieli et al., 2022; Maranna et al., 2024; Rao & Deka, 2024; Shoaib et al., 2020; Tsegaye et al., 2025). This extensive literature is notwithstanding a considerable number of numeric papers that are structured around a small number of one-factor-at-a-time profile plots. These physical plots give information in a physical way, without quantifying that the control parameters relative to each other in some parameter space with a design, and they do not test interactions, and rarely do such plots make a primary dataset available in an independent statistical way. This limitation is addressed in the present study by providing a factorial computational design and SPSS-compatible response-surface analysis in couple with the classical similarity analysis. It is not to consider the deterministic simulations as a random population sample; instead, regression and ANOVA are the response-surface screening methods to measure the effect size, interaction, curvature and predictive quality within the explicitly defined design space.

2. Significant Review of Literature

Four streams interlock to be seen as the literature. The former is related to the kinematics of stretching surfaces. Following a linear stretching solution given by Crane (1970) the exponential and nonlinear stretching stretching solution were studied since the speed of the local surfaces in actual manufacturing can change sharply with distance. Magyari and Keller (1999) worked out solutions showing heat and mass transfer of exponentially stretching surfaces; Khan and Sanjayanand (2005) and Sanjayanand and Khan (2006) generalized the use of exponential stretching to viscoelastic transport and Cortell (2007, 2008b, 2011) has studied nonlinear stretching that includes thermal effects and the effects of fluid properties. Afzal (2010), Prasad et al. (2010), and Nandeppanavar et al. (2011) have also demonstrated that both the momentum and energy transport are redefined by the stretching exponent, the properties of variable and the non-uniform sources of heat. The mathematical sensitivity of similarity solutions to the stretching law and thermal boundary specification was defined by this stream. The second one is related to the nanofluid transport. Masuda et al. (1993) reported an alteration of the transport characteristics of ultra-fine particle suspensions and Khanafer et al. (2003) and Oztop and Abu-Nada (2008) revealed the modification of heat-transfer in the envelopment of nanofluid due to buoyancy. Buongiorno (2006) model provided a mechanistic explanation as to the migration of particles and the studies done subsequently by Kuznetsov-Nield (2010) and Nield-Kuznetsov (2009, 2011) introduced the role of nanofluid transport in the boundary-layer and porous-media convection. In the case of stretching surfaces, a widely used formulation was given by Khan and Pop (2010) which was followed by the convective boundary conditions, slip, exponential stretching application as well as finite-elements applications (Makinde and Aziz, 2011; Nadeem and Lee, 2012; Noghrehabadi et al., 2012; Rana and Bhargava, 2012). All these studies showed that the concentration of nanoparticles and the property or transport model adopted may alter the wall heat transfer and concentration profiles, but the direction and the extent is dependent on the model. The 3rd stream is a combination of thermal and MHD. The studies of Hamad (2011), Kandasamy et al. (2011), and Ibrahim and Shankar (2013) demonstrated that the magnetic forces have the capability to reduce the momentum transport of the nanofluids over the stretching surfaces to a significant extent. The release of radiation was then combined with the MHD nanofluid models by Shakhaoath Khan et al. (2013), Shateyi and Prakash (2014), and Rashidi et al. (2014). Using the radiative diffusion interaction of radiant conductivity with nanoparticle-modified conductivity, Hady et al. (2012) explicitly applied the Rosseland approximation to a radiative problem of nanofluids in stretching and explained its effect on nanoparticle-laden fluid radiant diffusion. The subsequent researches added by non-Newtonian fluids and more complicated heating methods. Prasannakumara et al. (2017) emphasized nonlinear radiation in the presence of Sisko nanofluid, Bouslimi et al. (2021) took into consideration Joule heating and nonlinear radiation in the presence of Williamson nanofluid, and Alrihieli et al. (2022) investigated the radiative MHD nanofluid flow with convective heating and viscous dissipation. These findings confirm the relevance of radiation, however, inter-paper comparisons should be done with caution as some of them may be defining the radiation parameter as a conductivity ratio and others as its inverse. The fourth line is the new move of hybrid nanofluids, multiphysics and numerical optimization. The study by Devi and Devi

(2016) focused on a $Cu–Al_2O_3$/water hybrid nanofluid, and Yashkun et al. (2020) used the thermal radiation in MHD hybrid flow question between permeable stationary sheet stretching/shrinking. Shoaib et al. (2020) numerically examined rotating radiative MHD hybrid nanofluid flow, Mahabaleshwar et al. (2021) examined the porous-medium transport, and Waqas et al. (2022) compared the behaviour of the heat transfer in a thermally radiating hybrid system. More current researches include skin-friction control, Navier slip, nonlinear stretching, mixed convection, transport of microorganisms, Cattaneo–Christov fluxes, and response modeling (Maranna et al., 2024; Naseem and Kasana, 2024; Rao and Deka, 2024; Rauf et al., 2023; Tsegaye et al., 2025; Vishalakshi et al., 2023). Very new research is ongoing to the higher-order hybrid systems, and data-assisted response prediction (Abbas et al., 2026; Imran et al., 2026; Kavitha et al., 2026). Another significant strand is that of numerical technique. It has been integrated by shooting with Runge Kutta integration, finite difference, finite elements, homotopy methods, collocation boundary-value solvers as well as spectral methods. An acceptable MHD-nanofluid experiment ought to thus exhibit mesh/domain adequacy or benchmark agreement as opposed to just exhibiting convergence of a black-box solver. For nonlinear stretching nanofluids, Rana and Bhargava (2012) provided a numerical treatment; Shateyi and Prakash (2014) used a numerically based approach of boundaryvalues; Rao and Deka (2022) used a numerical analysis of a radiative MHD hybrid; and Rao and Deka (2024) numerically analyzed a radiative MHD hybrid problem. The new opportunity is to supplement solver validation with specific computational experiments and statistical response analysis so that the numerical model can provide not merely with the answer to the question what does a profile look like but also with the answer to the question which parameter is most important, how significant, and interacts with other parameters in the domain considered?'

3. Research Gap

Synthesis of the literature reveals four connected gaps. First, many stretching-sheet studies rely on selected one-factor-at-a-time profiles, which do not provide a complete ranking of magnetic, radiation, and nanoparticle effects over a defined multidimensional domain. Second, main effects are often described qualitatively without a fitted response surface capable of separating linear effects, curvature, and interactions. Third, numerical wall quantities are not always accompanied by an exact or external benchmark, making it difficult to distinguish physical trends from solver error. Fourth, primary computational data and analysis-ready files are rarely supplied in a form that permits independent re-analysis. The present study addresses these gaps with a complete 5 × 5 × 5 deterministic design (125 converged solutions), exact limiting-case validation, transparent reporting of wall-response definitions, and SPSS-compatible descriptive and response-surface analysis. The statistical layer is used to quantify geometry of the deterministic response surface, not to imply random sampling from a physical population.

3.1 Novelty and Contributions

The novelty lies in the combined workflow rather than in introducing an additional transport term. The study converts the full M–Rd–φ parameter domain into an auditable computational design, validates the numerical solver against an exact MHD wall-shear benchmark, and then quantifies main effects, curvature, and two-factor interactions from all 125 converged design points rather than from a small collection of illustrative profiles.

A second contribution is the explicit separation between the local dimensionless wall-temperature gradient, $-\theta'(0)$, and the reported reduced total Nusselt response, which multiplies that gradient by the combined conductive-plus-radiative conductivity factor. This distinction removes the apparent contradiction in which stronger radiation can produce a thicker thermal boundary layer while simultaneously increasing total wall heat transfer under the additive radiation convention used here.

A third contribution is reproducibility: the complete computational matrix and SPSS-compatible syntax are supplied so that effect ranking and response-surface results can be independently checked. The framework is therefore positioned as a bridge between classical similarity analysis and design-based surrogate modeling for subsequent optimization, uncertainty analysis, and model comparison.

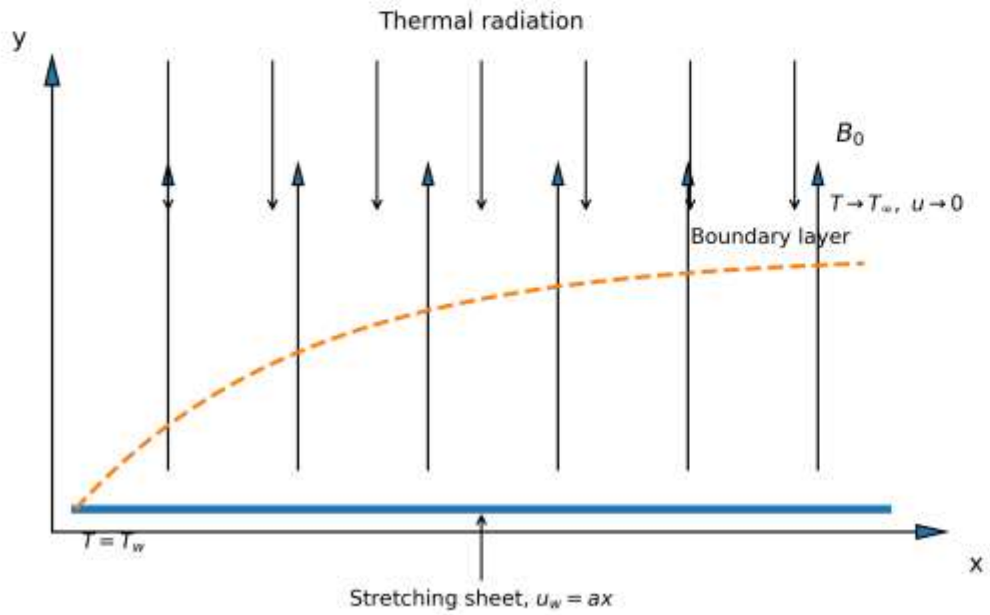

Figure 1. Physical configuration of the radiative MHD nanofluid boundary layer over a stretching sheet (original schematic prepared for this study).

4. Research Questions, Objectives, Data Objectives, and Hypotheses

4.1 Research Questions

For clarity, the two wall quantities are referred to below as reduced wall drag and reduced total Nusselt response; their formal mathematical definitions are given in Section 6.

- RQ1: How does the magnetic parameter M modify the dimensionless velocity profile $f'(\eta)$ and the reduced wall-drag response C_f^* over the prescribed design space?
- RQ2: How does the radiation parameter Rd modify the temperature profile $\theta(\eta)$, the wall-temperature gradient $-\theta'(0)$, and the reduced total Nusselt response Nu^* under the additive radiative-conductivity definition used in this study?
- RQ3: What are the marginal effects of the Al_2O_3 nanoparticle volume fraction φ on C_f^* and Nu^* for $0 \le \varphi \le 0.04$?
- RQ4: How do the two-factor interactions M × Rd, M × φ, and Rd × φ modify the in-domain prediction of Nu^* beyond the main effects?
- RQ5: How accurately does a second-order response-surface model reproduce the 125 deterministic Nu^* values within the tested parameter domain?

4.2 Research Objectives

- To formulate and numerically solve the similarity-reduced MHD momentum and radiative energy equations for an Al_2O_3–water nanofluid over a linearly stretching sheet.

- To quantify changes in $f'(\eta)$, $\theta(\eta)$, C_f^*, and Nu^* over a complete three-factor computational design in M, Rd, and φ.
- To validate the numerical wall-shear solution against the exact Newtonian MHD stretching-sheet limiting relation.
- To rank the design-space contributions of M, Rd, and φ using descriptive correlations and SPSS-compatible regression coefficients while explicitly recognizing the deterministic nature of the runs.
- To construct a second-order response-surface model for Nu^* and evaluate curvature, two-factor interactions, and in-domain predictive fidelity.

4.3 Data-Analysis Objectives

The complete set of converged solutions is organized as a transparent computational dataset with one row for each prescribed parameter combination.

To calculate descriptive statistics, Pearson design-space correlations, first-order regression coefficients, model-fit quantities, and second-order response-surface terms from the 125-run factorial grid.

To interpret coefficient magnitude, direction, interaction, curvature, and numerical fit as properties of the deterministic design surface. Nominal p values are retained only as conventional term-screening diagnostics and are not used to generalize to a randomly sampled population.

4.4 Hypotheses

- H1: Within the tested domain, increasing M increases reduced wall drag; equivalently, the design-space slope satisfies $\partial C_f^*/\partial M > 0$.
- H2: Within the tested domain, increasing M decreases the reduced total Nusselt response; equivalently, $\partial Nu^*/\partial M < 0$.
- H3: Under the present additive radiation definition, increasing Rd increases the reduced total Nusselt response; equivalently, $\partial Nu^*/\partial Rd > 0$ over the tested range.
- H4: Over $0 \le \varphi \le 0.04$, the marginal effects of nanoparticle loading on both C_f^* and Nu^* are positive, while the magnitude of the Nu^* effect may depend on M and Rd through interaction terms.
- H5: At least one two-factor interaction among M × Rd, M × φ, and Rd × φ materially improves the second-order in-domain representation of Nu^* beyond the main-effects model.
- H6: The second-order response-surface model for the 125 deterministic Nu^* values will achieve adjusted $R^2 > 0.95$ within the specified design space.

5. Methodology

This study uses a deterministic computational design rather than a random experiment. Primary data are the numerical outputs generated by the specified governing equations at predetermined combinations of M, Rd, and φ. Accordingly, N = 125 refers to 125 computational design points (converged boundary-value solutions), not to 125 independently sampled experimental observations. Statistical summaries are used to describe and screen the geometry of the computed response surface within the stated domain.

- Research design: Complete 5 × 5 × 5 factorial computational grid, giving 125 distinct converged boundary-value solutions.
- Fluid system: Al_2O_3 nanoparticles dispersed in water and represented by a single-phase effective-property model for density, volumetric heat capacity, Brinkman viscosity, and Maxwell thermal conductivity.

- Control parameters: M = 0, 0.5, 1.0, 1.5, 2.0; Rd = 0, 0.5, 1.0, 1.5, 2.0; φ = 0, 0.01, 0.02, 0.03, 0.04; Pr = 6.2 held constant.
- Outcomes and numerical solution: The primary wall responses are $C_f^* = C_f\sqrt{Re_x}$ and $Nu^* = Nu_x/\sqrt{Re_x}$. The nonlinear similarity equations were solved on $0 \le \eta \le 12$ with an adaptive collocation boundary-value algorithm using a tolerance of 10^{-6}; far-field boundary conditions were imposed at the truncated boundary η = 12.
- Validation: For the Newtonian limiting case φ = 0, the computed wall-shear magnitude $-f''(0)$ was compared with the exact stretching-sheet MHD relation $\sqrt{(1 + M)}$. The maximum absolute percentage error over M = 0–2 was below 0.001%.
- SPSS-compatible analysis: The 125-row data matrix can be imported directly into IBM SPSS Statistics. Descriptive statistics, Pearson correlations, ordinary least-squares coefficients, model-fit summaries, and a second-order response surface were calculated with mathematically equivalent routines; reproducible SPSS syntax is provided in Appendix B. Because the design points are deterministic, effect size, direction, interaction structure, residual fit, and numerical validation carry the primary interpretive weight. Any p values reported at α = .05 are nominal model-term screening quantities, not sampling-based evidence about a wider population.

6. Mathematical Formulation and Numerical Procedure

Consider steady, incompressible, two-dimensional flow above a flat sheet stretched with velocity $u_w = ax$, where $a > 0$. A uniform transverse magnetic field B_0 is applied normal to the sheet. The induced magnetic field, streamwise pressure gradient, viscous dissipation, and Joule heating are neglected in the baseline formulation so that the effects of magnetic braking, additive Rosseland radiation, and nanoparticle-induced effective-property changes can be isolated. The ambient fluid is quiescent at temperature T_∞, and the sheet temperature is T_w.

$$\eta = y\sqrt{\frac{a}{\nu_f}}$$

$$\psi = x\sqrt{a\nu_f}\, f(\eta), \qquad u = axf'(\eta), \qquad v = -\sqrt{a\nu_f}\, f(\eta)$$

$$\theta(\eta) = \frac{T - T_\infty}{T_w - T_\infty}$$

$$Af''' + ff'' - (f')^2 - Mf' = 0$$

$$\theta'' + Gf\theta' = 0$$

$$A = \frac{\mu_{nf}/\mu_f}{\rho_{nf}/\rho_f}$$

$$G = \frac{\mathrm{Pr}\left[(\rho c_p)_{nf}/(\rho c_p)_f\right]}{k_{nf}/k_f + \mathrm{Rd}}$$

The boundary conditions are

$$f(0) = 0, \quad f'(0) = 1, \quad \theta(0) = 1, \quad f'(\infty) = 0, \quad \theta(\infty) = 0$$

The single-phase effective properties are

$$\rho_{nf} = (1 - \phi)\rho_f + \phi\rho_s$$

$$(\rho c_p)_{nf} = (1 - \phi)(\rho c_p)_f + \phi(\rho c_p)_s$$

$$\mu_{nf} = \frac{\mu_f}{(1-\phi)^{2.5}}$$

$$\frac{k_{nf}}{k_f} = \frac{k_s + 2k_f - 2\phi(k_f - k_s)}{k_s + 2k_f + \phi(k_f - k_s)}$$

This effective-property formulation is intentionally simpler than a two-component Buongiorno transport model. In the present radiation convention, Rd is the radiative-conductivity contribution normalized by the base-fluid conductivity. Thus, the energy equation and the wall heat-flux definition use the sum of the nanofluid conductivity ratio and Rd. Some publications use a reciprocal radiation parameter; direct comparisons therefore require checking the definition before comparing trends.

$$Re_x = \frac{u_w x}{\nu_f} = \frac{a x^2}{\nu_f}$$

$$C_f\sqrt{Re_x} = \frac{\mu_{nf}}{\mu_f}[-f''(0)]$$

$$\frac{Nu_x}{\sqrt{Re_x}} = \left(\frac{k_{nf}}{k_f} + \mathrm{Rd}\right)[-\theta'(0)]$$

This definition is central to interpreting the radiation results. Increasing Rd raises the effective thermal diffusivity and produces a warmer, thicker dimensionless thermal layer, which reduces the magnitude of the local wall gradient $-\theta'(0)$. At the same time, Rd directly increases the multiplicative conductive-plus-radiative factor in Nu^*. Over the present design domain, the increase in that factor is larger than the reduction in $-\theta'(0)$, so the reported total reduced Nusselt response increases with Rd. Thus, "higher temperature profile" and "higher total wall heat transfer" are not contradictory under this convention.

7. Results and Data Analysis

7.1 Numerical Validation

Table 1. Validation of reduced wall shear for the Newtonian limiting case

M	**Exact √(1+M)**	**Numerical**	**Absolute error (%)**
0.0	1.000000	1.000001	0.000113
0.5	1.224745	1.224745	0.000000
1.0	1.414214	1.414214	0.000000
1.5	1.581139	1.581139	0.000000
2.0	1.732051	1.732051	0.000000

Note. The solver reproduces the exact stretching-sheet MHD wall-shear relation to better than 0.001% over the tested range.

Agreement in Table 1 is within the stated reporting precision. This benchmark is important because the same collocation framework generated the complete factorial dataset. The validation confirms that the increase in wall-shear magnitude with M is a property of the governing momentum equation rather than a numerical artifact.

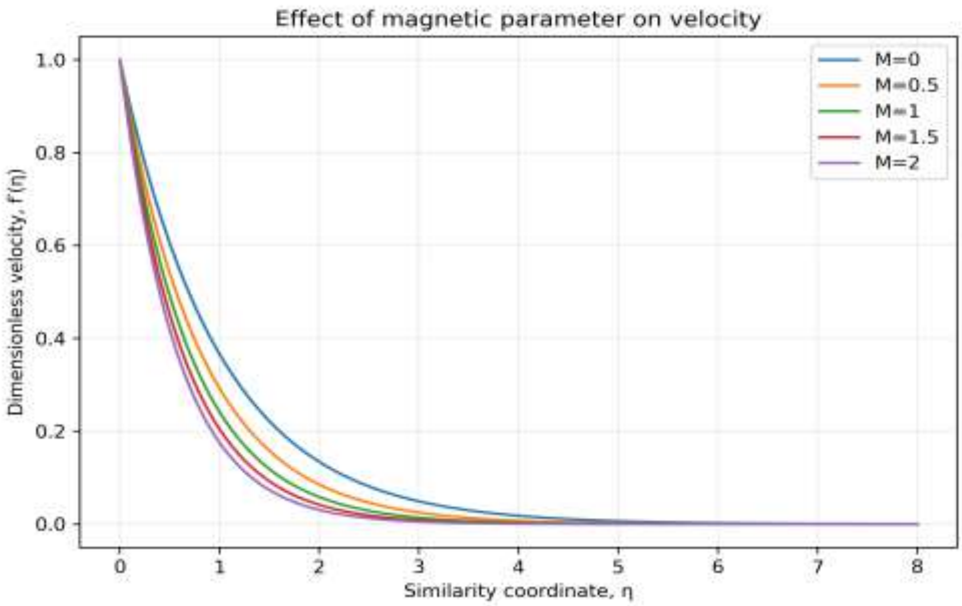

Figure 2. Effect of magnetic parameter M on the dimensionless velocity profile at Rd = 1 and φ = .02.

Figure 2 shows that the dimensionless streamwise velocity $f'(\eta)$ is monotonically suppressed as M increases. The stronger transverse magnetic field increases Lorentz resistance, causing the velocity to decay more rapidly away from the stretching sheet. At the same time, the magnitude of the wall velocity gradient $-f''(0)$ increases; therefore, the reduced skin-friction magnitude C_f^* increases with M. This behavior is consistent with established MHD stretching-sheet results (Hamad, 2011; Ibrahim & Shankar, 2013; Kandasamy et al., 2011).

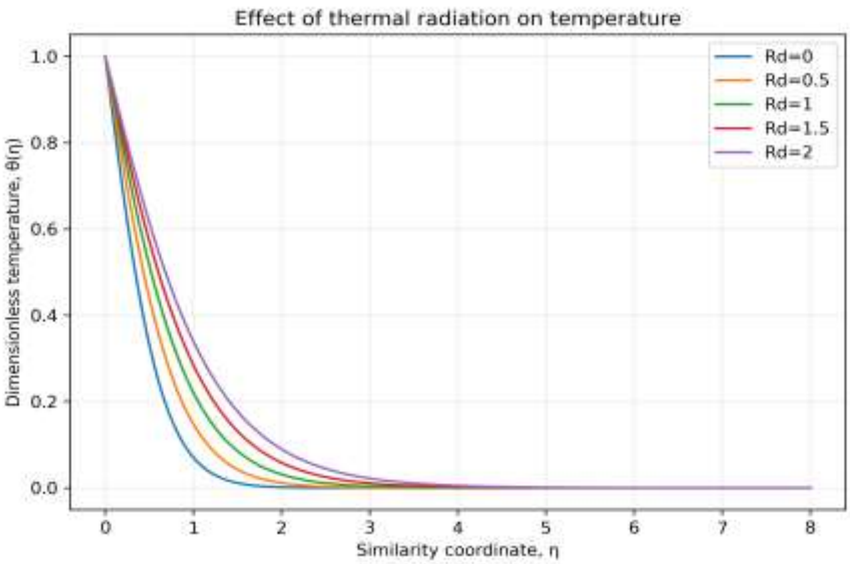

Figure 3. Effect of radiation parameter Rd on the dimensionless temperature profile at M = 1 and φ = .02.

Figure 3 must be interpreted together with the definition of Nu^*. As Rd increases, $\theta(\eta)$ decays more slowly, indicating a thicker and warmer thermal boundary layer and a smaller magnitude of the local dimensionless wall-temperature gradient $-\theta'(0)$. However, Nu^* is not equal to $-\theta'(0)$ alone; it is defined as $(k_{nf}/k_f + Rd)[-\theta'(0)]$. In the present calculations, the increase in the conductive-plus-radiative multiplier more than compensates for the reduced gradient, so the total reduced wall heat-transfer response increases with Rd. All subsequent radiation results use this total-flux definition.

7.2 Descriptive Statistics of the Primary Computational Data

Table 2. Descriptive statistics for the 125-run design

Variable	Mean	SD	Minimum	Maximum
Magnetic parameter (M)	1.0000	0.7100	0.0000	2.0000
Radiation parameter (Rd)	1.0000	0.7100	0.0000	2.0000
Volume fraction (φ)	0.0200	0.0142	0.0000	0.0400
Reduced wall drag	1.4686	0.2797	1.0000	1.9284
Reduced total Nusselt response	2.1773	0.3178	1.6108	2.8092

Note. N = 125 for every variable. Values are deterministic simulation outputs across the complete factorial grid.

Across the 125 design points, C_f^* ranges from 1.0000 to 1.9284 and Nu^* from 1.6108 to 2.8092. Marginal means show a clear magnetic trade-off: increasing M from 0 to 2 raises mean C_f^* from 1.0562 to 1.8294 (+73.2%) while lowering mean Nu^* from 2.3502 to 2.0286 (−13.7%). Increasing Rd from 0 to 2 leaves C_f^* unchanged in this baseline momentum model and raises mean Nu^* from 1.7184 to 2.5467 (+48.2%). Increasing φ from 0 to 0.04 raises mean C_f^* from 1.3904 to 1.5480 (+11.3%) and mean Nu^* from 2.1613 to 2.1938 (+1.5%). Thus, radiation produces the largest positive marginal change in the reported total Nusselt response, whereas nanoparticle loading produces a much smaller positive marginal heat-transfer change together with a clearer drag penalty.

Table 3. Marginal means across factor levels

Factor level	Mean C_f^*	Mean Nu^*
M=0	1.0562	2.3502
M=0.5	1.2936	2.2493
M=1	1.4937	2.1654
M=1.5	1.6700	2.0928
M=2	1.8294	2.0286
Rd=0	1.4686	1.7184
Rd=0.5	1.4686	2.0021
Rd=1	1.4686	2.2209
Rd=1.5	1.4686	2.3983
Rd=2	1.4686	2.5467
φ=0.00	1.3904	2.1613
φ=0.01	1.4288	2.1690
φ=0.02	1.4679	2.1770
φ=0.03	1.5076	2.1853
φ=0.04	1.5480	2.1938

Note. Each M or Rd mean averages 25 runs; each φ mean also averages 25 runs.

7.3 Design-Space Correlation Analysis

Table 4. Pearson correlation matrix

Item	M	Rd	φ	C_f^*	Nu^*
M	1.000	0.000	0.000	0.976	-0.357
Rd	0.000	1.000	0.000	0.000	0.917
φ	0.000	0.000	1.000	0.200	0.036
C_f^*	0.976	0.000	0.200	1.000	-0.344
Nu^*	-0.357	0.917	0.036	-0.344	1.000

Note. Because M, Rd, and φ were factorially orthogonal, their mutual correlations are approximately zero. Correlations with the outputs therefore provide clear first-order effect ranking.

Because M, Rd, and φ are orthogonal in the complete factorial grid, the Pearson coefficients provide a transparent first-order ranking of linear design-space associations. M is strongly associated with higher C_f^* (r = .976) and moderately associated with lower Nu^* (r = −.357). Rd has no direct association with C_f^* in the baseline momentum equation and is the dominant positive first-order correlate of Nu^* (r = .917). The marginal correlation between φ and Nu^* is small (r = .036), whereas its correlation with C_f^* is larger (r = .200). These are deterministic design summaries, not estimates of population correlations, and the small marginal φ–Nu^* coefficient should be read together with the interaction terms in Section 7.5.

7.4 SPSS-Compatible Regression Screening and Directional Hypothesis Assessment

Table 5. First-order regression model for reduced skin-friction magnitude

Predictor	B	SE B	β	t	p
Constant	1.0052	0.0058	—	173.91	< .001
M	0.3846	0.0031	0.976	124.47	< .001
Rd	0.0000	0.0031	0.000	0.00	1.000
φ	3.9394	0.1545	0.200	25.50	< .001

Note. $R^2 = 0.9926$; adjusted $R^2 = 0.9924$; $F(3, 121) = 5381.07$, nominal $p < .001$. p values are reported only as deterministic model-term screening diagnostics.

Table 6. First-order regression model for reduced total Nusselt response

Predictor	B	SE B	β	t	p
Constant	1.9104	0.0131	—	146.02	< .001
M	-0.1599	0.0070	-0.357	-22.87	< .001
Rd	0.4106	0.0070	0.917	58.71	< .001
φ	0.8146	0.3497	0.036	2.33	0.021

Note. $R^2 = 0.9705$; adjusted $R^2 = 0.9697$; $F(3, 121) = 1325.12$, nominal $p < .001$. p values are reported only as deterministic model-term screening diagnostics.

The first-order wall-drag model reproduces 99.26% of the variation across the deterministic grid. M is the dominant standardized coefficient (β = .976), followed by φ (β = .200), while Rd is exactly null in this baseline momentum specification because radiation does not enter the momentum equation. The first-order Nu^* model reproduces 97.05% of the design variation. Rd is the largest positive standardized coefficient (β = .917), M is negative (β = −.357), and φ is small but positive (β = .036). Under the stated screening convention, the corresponding nominal p values are < .001 for M and Rd and .021 for φ in the Nu^* model. These coefficients support H1–H4 within the tested computational domain; they are not population-level causal estimates.

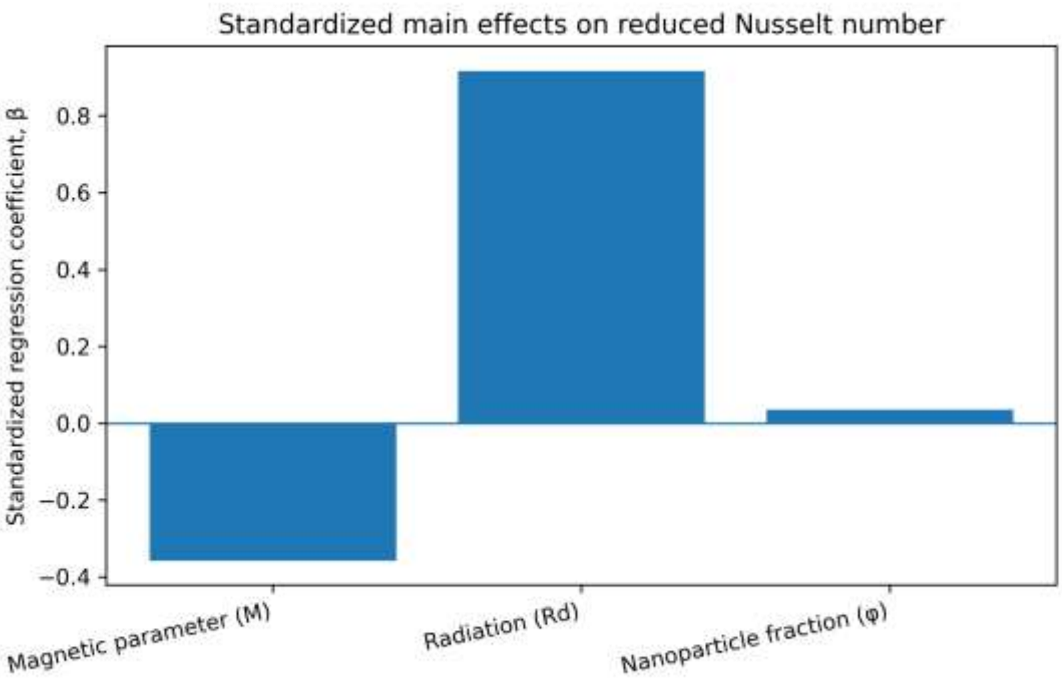

Figure 4. Standardized first-order regression coefficients of M, Rd, and φ for the reduced total Nusselt response.

7.5 Interaction and Quadratic Response-Surface Analysis

Table 7. Second-order response-surface coefficients for reduced total Nusselt response

Term	B	p
M	-0.1297	< .001
Rd	0.6766	< .001
φ	1.6821	< .001
M^2	0.0242	< .001
Rd^2	-0.0892	< .001
$φ^2$	1.4662	0.699
M × Rd	-0.0739	< .001
M × φ	-0.2349	< .001
Rd × φ	-0.6913	< .001

Note. Model $R^2 = 0.9995$; adjusted $R^2 = 0.9995$; $F(9, 115) = 27750.22$, nominal $p < .001$. Coefficients are unstandardized over the physical parameter values in Section 5; p values are screening diagnostics for this deterministic design.

The quadratic response surface achieves adjusted $R^2 = 0.9995$, clearly exceeding the prespecified H6 criterion of 0.95. The curvature terms M^2 and Rd^2 are retained under the nominal screening convention (p

< .001), whereas φ^2 is not ($p = .699$). All three two-factor interaction coefficients are negative: M × Rd = −0.0739, M × φ = −0.2349, and Rd × φ = −0.6913 (nominal $p < .001$ for each). The negative M × Rd coefficient does not mean that radiation reduces Nu^*; rather, it means that the incremental gain in Nu^* produced by increasing Rd becomes smaller as M increases. Likewise, the interactions involving φ show that its small positive marginal heat-transfer effect is condition-dependent. The interaction structure supports H5 and demonstrates why one-factor profiles alone are insufficient to characterize the full response surface.

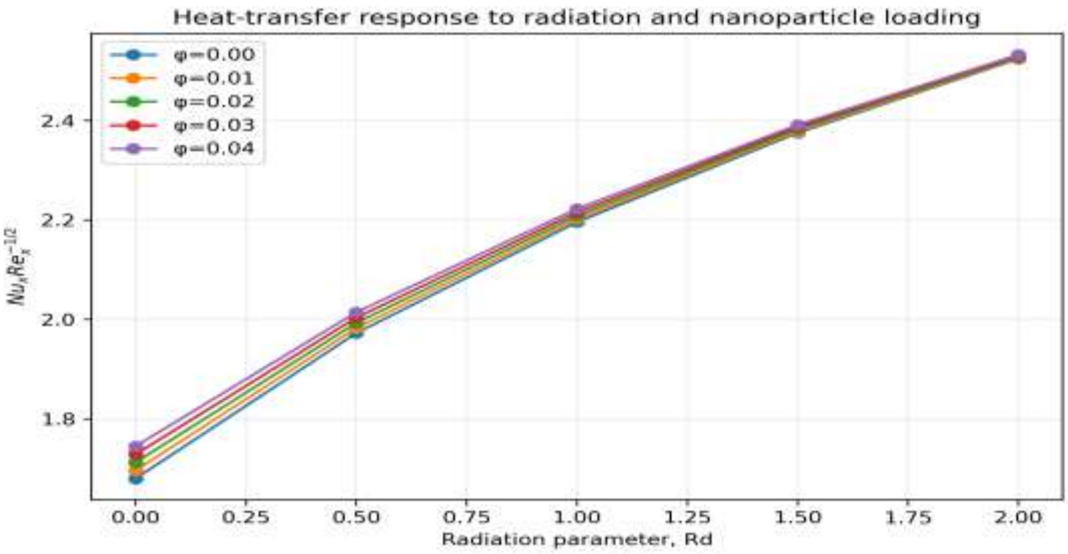

Figure 5. Reduced total Nusselt number versus radiation parameter for five nanoparticle loadings at M = 1.

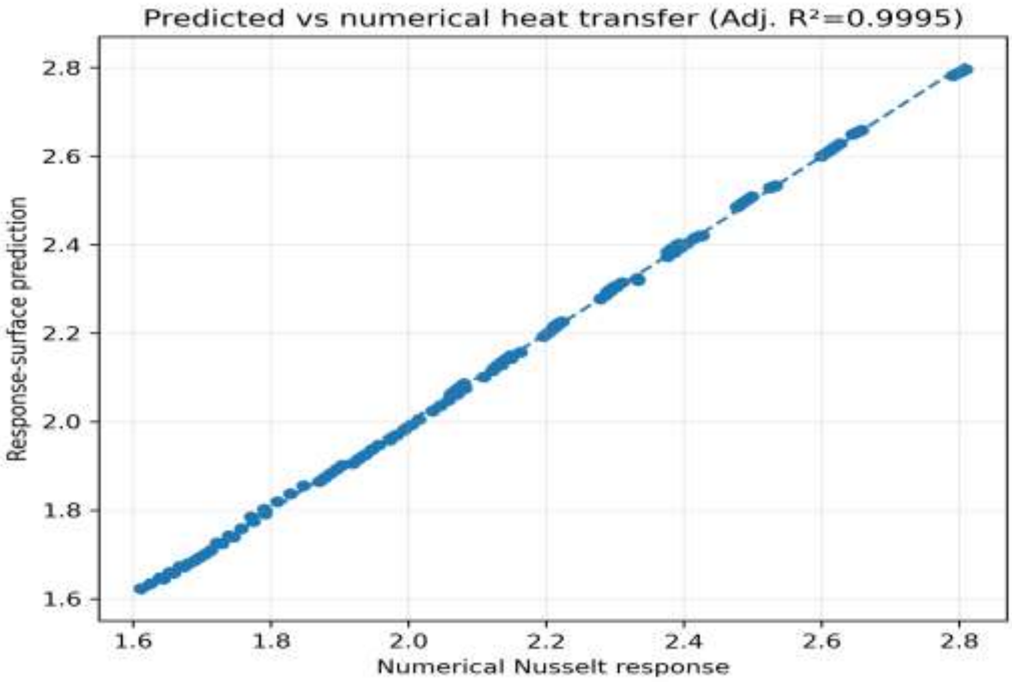

Figure 6. Agreement between numerical heat-transfer responses and second-order response-surface predictions.

Figure 5 makes the radiation trend unambiguous at M = 1: Nu^* increases with Rd for each plotted nanoparticle loading. The separation among the φ curves is comparatively small, consistent with the weak marginal φ effect, while the quadratic model shows that the local φ slope varies with M and Rd. Figure 6 shows near-identity agreement between the 125 numerical Nu^* values and the second-order fitted values. The response surface is therefore a high-fidelity in-domain surrogate over $0 \leq M \leq 2$, $0 \leq Rd \leq 2$, and $0 \leq \varphi \leq 0.04$; extrapolation beyond these limits is not justified without new numerical runs.

Table 8. Hypothesis decisions

Hypothesis	**Expectation**	**Decision**	**Key evidence**
H1	M increases C_f^*	Supported in design space	$\beta = .976$; nominal $p < .001$
H2	M decreases Nu^*	Supported in design space	$\beta = -.357$; nominal $p < .001$
H3	Rd increases Nu^* under the stated total-flux definition	Supported in design space	$\beta = .917$; nominal $p < .001$
H4	φ has positive marginal effects on C_f^* and Nu^* over 0–0.04	Supported in tested range	Positive first-order coefficients; interaction-modulated Nu^* slope
H5	At least one two-factor interaction materially improves the quadratic Nu^* model	Supported in design space	All three interaction terms retained; nominal $p < .001$
H6	Quadratic model adjusted $R^2 > .95$	Supported	Adjusted $R^2 = .9995$

Note. Decisions apply only to the specified deterministic computational design space. "Supported" refers to directional and model-fit consistency within that grid, not to population-level causal inference.

8. Discussion

The combined numerical and response-surface results provide a coherent physical picture of the present MHD stretching-sheet model. Increasing M suppresses $f'(\eta)$ through Lorentz braking, steepens the wall velocity gradient, and increases C_f^*. At the same time, the marginal Nu^* response decreases with M. This magnetic trade-off agrees with the broad behavior reported in MHD stretching-sheet studies, although the magnitude of the effect depends on the precise energy model and property assumptions (Hamad, 2011; Ibrahim & Shankar, 2013; Kandasamy et al., 2011; Mabood et al., 2015). Rd has no direct effect on wall drag here because no radiation-dependent term appears in the momentum equation.

Radiation is the dominant positive driver of the reported total heat-transfer response, but this result must be stated with the present normalization. A larger Rd increases effective thermal diffusion, so $\theta(\eta)$ remains higher farther from the wall and the local gradient magnitude $-\theta'(0)$ decreases. Nevertheless, the total reduced Nusselt response multiplies this gradient by the combined conductive-plus-radiative conductivity factor. That factor increases sufficiently rapidly that the total response rises throughout the tested Rd range.

Consequently, the statements "radiation thickens the thermal boundary layer" and "radiation increases total wall heat transfer" are simultaneously true in this formulation. Comparisons with other studies should therefore verify whether their radiation parameter is defined additively, reciprocally, or with a different Nusselt normalization (Hady et al., 2012; Rashidi et al., 2014; Sajid & Hayat, 2008; Shateyi & Prakash, 2014).

Nanoparticle loading produces a more modest thermal benefit. From $\varphi = 0$ to 0.04, the marginal mean Nu^* increases by about 1.5%, while C_f^* increases by about 11.3%. This reflects competing effective-property changes: Maxwell conductivity increases, but viscosity and volumetric heat capacity also change. The negative $M \times \varphi$ and $Rd \times \varphi$ coefficients further show that the local benefit of increasing φ is not strictly additive across all magnetic and radiation conditions. The practical implication is that nanoparticle loading should be assessed against its drag penalty rather than treated as an automatically beneficial heat-transfer control (Buongiorno, 2006; Khan & Pop, 2010; Makinde & Aziz, 2011; Noghrehabadi et al., 2012).

Methodologically, the main contribution is the replacement of sparse profile-based interpretation with a complete factorial computational dataset and a compact response-surface representation. The first-order standardized coefficients provide effect ranking, while the quadratic model exposes curvature and interactions that are hidden in one-factor plots. In particular, the negative $M \times Rd$ coefficient means that radiation remains beneficial for Nu^* but its incremental benefit diminishes as magnetic braking becomes stronger. The adjusted $R^2 = 0.9995$ therefore indicates excellent in-domain reproduction of the computed surface; it should not be interpreted as evidence of statistical generalizability beyond the modeled equations or parameter limits.

Several limitations define the scope of the conclusions. The single-phase effective-property model does not resolve Brownian diffusion, thermophoresis, particle agglomeration, or an independent nanoparticle concentration field. Non-Newtonian rheology, temperature-dependent properties, induced magnetic field, viscous dissipation, Joule heating, and slip are omitted. The linearized Rosseland approximation is most appropriate for optically thick media with moderate temperature differences. Most importantly, the 125 runs are deterministic computational design points; nominal regression p values reflect model residual geometry rather than repeated-sampling uncertainty. Future work should combine the present reproducible response-surface workflow with richer transport models, property uncertainty, hybrid nanofluids, and multiobjective optimization of heat-transfer enhancement against frictional penalty.

9. Conclusion

This study developed a reproducible numerical and deterministic response-surface analysis of radiative MHD Al_2O_3–water nanofluid flow over a linearly stretching surface. A complete M–Rd–φ factorial grid produced 125 converged boundary-value solutions, and the wall-shear solver matched the exact Newtonian MHD benchmark to within 0.001%. Within the tested domain, M is the dominant positive driver of reduced wall drag and a negative driver of the reduced total Nusselt response. Rd is the dominant positive driver of Nu^*: although it thickens the thermal boundary layer and reduces $-\theta'(0)$, the additive conductive-plus-radiative factor in Nu^* causes the total wall heat-transfer response to increase. Nanoparticle loading provides a much smaller positive marginal Nu^* effect while increasing drag. The first-order heat-transfer model gives $R^2 = 0.9705$, and the quadratic model gives adjusted $R^2 = 0.9995$ while capturing important $M \times Rd$, $M \times \varphi$, and $Rd \times \varphi$ interactions. These findings support the six directional/model hypotheses only within the specified deterministic design space. The strongest contribution of the paper is therefore the integrated framework: exact numerical validation, a complete analysis-ready computational dataset, unambiguous heat-flux definitions, and interaction-aware response-surface modeling that extends classical similarity plots into a reproducible basis for design and optimization.

Data Availability and Reproducibility Statement

The complete set of 125 deterministic computational design points used in the reported analyses is provided in Appendix A, and Appendix B supplies SPSS-compatible syntax for reproducing the descriptive statistics, correlations, and first-order regressions. The rows are outputs of the governing equations at prescribed parameter combinations; they are not random human, laboratory, or field observations. The dataset should therefore be interpreted as a reproducible numerical design surface rather than as a random sample from a physical population.

References

1. Abbas, S. T., Qureshi, I. H., Sohail, M., & Khan, M. J. (2026). Numerical investigation of Williamson nanofluid heat transfer over a stretching sheet employing Buongiorno model and Bvp4c boundary layer solution. Partial Differential Equations in Applied Mathematics, 18, 101362. https://doi.org/10.1016/j.padiff.2026.101362
2. Afzal, N. (2010). Momentum and thermal boundary layers over a two-dimensional or axisymmetric nonlinear stretching surface in a stationary fluid. International Journal of Heat and Mass Transfer, 53(1–3), 540–547. https://doi.org/10.1016/j.ijheatmasstransfer.2009.04.039
3. Alrihieli, H., Alrehili, M., & Megahed, A. M. (2022). Radiative MHD nanofluid flow due to a linearly stretching sheet with convective heating and viscous dissipation. Mathematics, 10(24), 4743. https://doi.org/10.3390/math10244743
4. Balogun, O. S., Aslam, M., Iqbal, M. Z., & Arshad, M. Z. (2025). Investigation of gold and silver based hybrid nanofluid with effects of thermal radiation over a stretching sheet. Alexandria Engineering Journal, 117, 352–363. https://doi.org/10.1016/j.aej.2025.01.031
5. Bhattacharyya, K., & Layek, G. C. (2014). Magnetohydrodynamic boundary layer flow of nanofluid over an exponentially stretching permeable sheet. Physics Research International, 2014, 592536. https://doi.org/10.1155/2014/592536
6. Bouslimi, J., Omri, M., Mohamed, R. A., Mahmoud, K. H., Abo-Dahab, S. M., & Soliman, M. S. (2021). MHD Williamson nanofluid flow over a stretching sheet through a porous medium under effects of Joule heating, nonlinear thermal radiation, heat generation/absorption, and chemical reaction. Advances in Mathematical Physics, 2021, 9950993. https://doi.org/10.1155/2021/9950993
7. Buongiorno, J. (2006). Convective transport in nanofluids. Journal of Heat Transfer, 128(3), 240–250. https://doi.org/10.1115/1.2150834
8. Cortell, R. (2007). Viscous flow and heat transfer over a nonlinearly stretching sheet. Applied Mathematics and Computation, 184(2), 864–873. https://doi.org/10.1016/j.amc.2006.06.077
9. Cortell, R. (2008a). Effects of viscous dissipation and radiation on the thermal boundary layer over a nonlinearly stretching sheet. Physics Letters A, 372(5), 631–636. https://doi.org/10.1016/j.physleta.2007.08.005
10. Cortell, R. (2008b). Similarity solutions for flow and heat transfer of a quiescent fluid over a nonlinearly stretching surface. Journal of Materials Processing Technology, 203(1–3), 176–183. https://doi.org/10.1016/j.jmatprotec.2007.09.055

11. Cortell, R. (2011). Heat and fluid flow due to non-linearly stretching surfaces. Applied Mathematics and Computation, 217(17), 7564–7572. https://doi.org/10.1016/j.amc.2011.02.029
12. Crane, L. J. (1970). Flow past a stretching plate. Zeitschrift für Angewandte Mathematik und Physik, 21, 645–647. https://doi.org/10.1007/BF01587695
13. Devi, S. P. A., & Devi, S. S. U. (2016). Numerical investigation of hydromagnetic hybrid Cu–Al_2O_3/water nanofluid flow over a permeable stretching sheet with suction. International Journal of Nonlinear Sciences and Numerical Simulation, 17(5), 249–257. https://doi.org/10.1515/ijnsns-2016-0037
14. Goyal, M., & Bhargava, R. (2014). Boundary layer flow and heat transfer of viscoelastic nanofluids past a stretching sheet with partial slip conditions. Applied Nanoscience, 4, 761–767. https://doi.org/10.1007/s13204-013-0254-5
15. Hady, F. M., Ibrahim, F. S., Abdel-Gaied, S. M., & Eid, M. R. (2012). Radiation effect on viscous flow of a nanofluid and heat transfer over a nonlinearly stretching sheet. Nanoscale Research Letters, 7, 229. https://doi.org/10.1186/1556-276X-7-229
16. Hamad, M. A. A. (2011). Analytical solution of natural convection flow of a nanofluid over a linearly stretching sheet in the presence of magnetic field. International Communications in Heat and Mass Transfer, 38(4), 487–492. https://doi.org/10.1016/j.icheatmasstransfer.2010.12.042
17. Hamad, M. A. A., & Pop, I. (2011). Scaling transformations for boundary layer stagnation-point flow towards a heated permeable stretching sheet in a porous medium saturated with a nanofluid and heat generation/absorption effects. Transport in Porous Media, 87, 25–39. https://doi.org/10.1007/s11242-010-9683-8
18. Ibrahim, S. M., Lakshmi, B. N., Maheswari, C., & Koten, H. (2025). Role of thermal radiation effect on unsteady dissipative MHD mixed convection of hybrid nanofluid over an inclined stretching sheet with chemical reaction. Frontiers in Heat and Mass Transfer, 23(5), 1555–1574. https://doi.org/10.32604/fhmt.2025.069392
19. Ibrahim, W., & Shankar, B. (2013). MHD boundary layer flow and heat transfer of a nanofluid past a permeable stretching sheet with velocity, thermal and solutal slip boundary conditions. Computers & Fluids, 75, 1–10. https://doi.org/10.1016/j.compfluid.2013.01.014
20. Imran, M., Ali, A. B. M., Farooq, U., Khan, S. A., Fatima, N., & Jia, W. (2026). Mathematical analysis of heat source/sink and thermal radiation effects on MHD hybrid nanofluid flow over a stretching surface. ZAMM - Journal of Applied Mathematics and Mechanics, 106(8), e70566. https://doi.org/10.1002/zamm.70566
21. Kandasamy, R., Loganathan, P., & Puvi Arasu, P. (2011). Scaling group transformation for MHD boundary-layer flow of a nanofluid past a vertical stretching surface in the presence of suction/injection. Nuclear Engineering and Design, 241(6), 2053–2059. https://doi.org/10.1016/j.nucengdes.2011.04.011
22. Kavitha, R., Samikannu, R., & Ladu, N. S. D. (2026). Numerical investigation of radiative chemically reactive induced-MHD Burgers' nanofluid flow over a nonlinear stretching sheet. Scientific Reports. https://doi.org/10.1038/s41598-026-61556-w
23. Khan, S. K., & Sanjayanand, E. (2005). Viscoelastic boundary layer flow and heat transfer over an exponential stretching sheet. International Journal of Heat and Mass Transfer, 48(8), 1534–1542. https://doi.org/10.1016/j.ijheatmasstransfer.2004.10.032

24. Khan, W. A., & Pop, I. (2010). Boundary-layer flow of a nanofluid past a stretching sheet. International Journal of Heat and Mass Transfer, 53(11–12), 2477–2483. https://doi.org/10.1016/j.ijheatmasstransfer.2010.01.032
25. Khanafer, K., Vafai, K., & Lightstone, M. (2003). Buoyancy-driven heat transfer enhancement in a two-dimensional enclosure utilizing nanofluids. International Journal of Heat and Mass Transfer, 46(19), 3639–3653. https://doi.org/10.1016/S0017-9310(03)00156-X
26. Kuznetsov, A. V., & Nield, D. A. (2010). Natural convective boundary-layer flow of a nanofluid past a vertical plate. International Journal of Thermal Sciences, 49(2), 243–247. https://doi.org/10.1016/j.ijthermalsci.2009.07.015
27. Mabood, F., Khan, W. A., & Ismail, A. I. M. (2015). MHD boundary layer flow and heat transfer of nanofluids over a nonlinear stretching sheet: A numerical study. Journal of Magnetism and Magnetic Materials, 374, 569–576. https://doi.org/10.1016/j.jmmm.2014.09.013
28. Madhu, J., Madhukesh, J. K., Sarris, I., Prasannakumara, B. C., Ramesh, G. K., Shah, N. A., Ali, B., Raju, C. S. K., Wakif, A., Muhammad, N., & Ashraf, H. (2024). Influence of quadratic thermal radiation and activation energy impacts over oblique stagnation point hybrid nanofluid flow across a cylinder. Case Studies in Thermal Engineering, 60, 104624. https://doi.org/10.1016/j.csite.2024.104624
29. Magyari, E., & Keller, B. (1999). Heat and mass transfer in the boundary layers on an exponentially stretching continuous surface. Journal of Physics D: Applied Physics, 32(5), 577–585. https://doi.org/10.1088/0022-3727/32/5/012
30. Mahabaleshwar, U. S., Anusha, T., & Hatami, M. (2021). The MHD Newtonian hybrid nanofluid flow and mass transfer analysis due to super-linear stretching sheet embedded in porous medium. Scientific Reports, 11, 22518. https://doi.org/10.1038/s41598-021-01902-2
31. Makinde, O. D., & Aziz, A. (2011). Boundary layer flow of a nanofluid past a stretching sheet with a convective boundary condition. International Journal of Thermal Sciences, 50(7), 1326–1332. https://doi.org/10.1016/j.ijthermalsci.2011.02.019
32. Maranna, T., Sachin, G. M., Mahabaleshwar, U. S., Pérez, L. M., & Shevchuk, I. V. (2024). Impact of Navier's slip and MHD on a hybrid nanofluid flow over a porous stretching/shrinking sheet with heat transfer. Fluids, 9(8), 180. https://doi.org/10.3390/fluids9080180
33. Masuda, H., Ebata, A., Teramae, K., & Hishinuma, N. (1993). Alteration of thermal conductivity and viscosity of liquid by dispersing ultra-fine particles. Netsu Bussei, 7(4), 227–233. https://doi.org/10.2963/jjtp.7.227
34. Nadeem, S., & Lee, C. (2012). Boundary layer flow of nanofluid over an exponentially stretching surface. Nanoscale Research Letters, 7, 94. https://doi.org/10.1186/1556-276X-7-94
35. Nandeppanavar, M. M., Vajravelu, K., Abel, M. S., & Ng, C.-O. (2011). Heat transfer over a nonlinearly stretching sheet with non-uniform heat source and variable wall temperature. International Journal of Heat and Mass Transfer, 54(23–24), 4960–4965. https://doi.org/10.1016/j.ijheatmasstransfer.2011.07.009
36. Naseem, A., & Kasana, A. G. (2024). Numerical assessment of MHD hybrid nanofluid flow over an exponentially stretching surface in the presence of mixed convection and non-uniform heat source/sink. Results in Engineering, 22, 102294. https://doi.org/10.1016/j.rineng.2024.102294

37. Nield, D. A., & Kuznetsov, A. V. (2009). The Cheng–Minkowycz problem for natural convective boundary-layer flow in a porous medium saturated by a nanofluid. International Journal of Heat and Mass Transfer, 52(25–26), 5792–5795. https://doi.org/10.1016/j.ijheatmasstransfer.2009.07.024
38. Nield, D. A., & Kuznetsov, A. V. (2011). The Cheng–Minkowycz problem for the double-diffusive natural convective boundary layer flow in a porous medium saturated by a nanofluid. International Journal of Heat and Mass Transfer, 54(1–3), 374–378. https://doi.org/10.1016/j.ijheatmasstransfer.2010.09.034
39. Noghrehabadi, A., Pourrajab, R., & Ghalambaz, M. (2012). Effect of partial slip boundary condition on the flow and heat transfer of nanofluids past stretching sheet prescribed constant wall temperature. International Journal of Thermal Sciences, 54, 253–261. https://doi.org/10.1016/j.ijthermalsci.2011.11.017
40. Oztop, H. F., & Abu-Nada, E. (2008). Numerical study of natural convection in partially heated rectangular enclosures filled with nanofluids. International Journal of Heat and Fluid Flow, 29(5), 1326–1336. https://doi.org/10.1016/j.ijheatfluidflow.2008.04.009
41. Partha, M. K., Murthy, P. V. S. N., & Rajasekhar, G. P. (2005). Effect of viscous dissipation on the mixed convection heat transfer from an exponentially stretching surface. Heat and Mass Transfer, 41, 360–366. https://doi.org/10.1007/s00231-004-0552-2
42. Prasad, K. V., Vajravelu, K., & Datti, P. S. (2010). Mixed convection heat transfer over a non-linear stretching surface with variable fluid properties. International Journal of Non-Linear Mechanics, 45(3), 320–330. https://doi.org/10.1016/j.ijnonlinmec.2009.12.003
43. Prasannakumara, B. C., Gireesha, B. J., Krishnamurthy, M. R., & Ganesh Kumar, K. (2017). MHD flow and nonlinear radiative heat transfer of Sisko nanofluid over a nonlinear stretching sheet. Informatics in Medicine Unlocked, 9, 123–132. https://doi.org/10.1016/j.imu.2017.07.006
44. Rana, P., & Bhargava, R. (2012). Flow and heat transfer of a nanofluid over a nonlinearly stretching sheet: A numerical study. Communications in Nonlinear Science and Numerical Simulation, 17(1), 212–226. https://doi.org/10.1016/j.cnsns.2011.05.009
45. Rao, S., & Deka, P. (2022). A numerical solution using EFDM for unsteady MHD radiative Casson nanofluid flow over a porous stretching sheet with stability analysis. Heat Transfer, 51(8), 8020–8042. https://doi.org/10.1002/htj.22679
46. Rao, S., & Deka, P. N. (2024). Numerical analysis of MHD hybrid nanofluid flow a porous stretching sheet with thermal radiation. International Journal of Applied and Computational Mathematics, 10, 95. https://doi.org/10.1007/s40819-024-01734-4
47. Rashidi, M. M., Vishnu Ganesh, N., Abdul Hakeem, A. K., & Ganga, B. (2014). Buoyancy effect on MHD flow of nanofluid over a stretching sheet in the presence of thermal radiation. Journal of Molecular Liquids, 198, 234–238. https://doi.org/10.1016/j.molliq.2014.06.037
48. Rauf, A., Shah, N. A., Mushtaq, A., & Botmart, T. (2023). Heat transport and magnetohydrodynamic hybrid micropolar ferrofluid flow over a non-linearly stretching sheet. AIMS Mathematics, 8(1), 164–193. https://doi.org/10.3934/math.2023008
49. Sajid, M., & Hayat, T. (2008). Influence of thermal radiation on the boundary layer flow due to an exponentially stretching sheet. International Communications in Heat and Mass Transfer, 35(3), 347–356. https://doi.org/10.1016/j.icheatmasstransfer.2007.08.006

50. Sakiadis, B. C. (1961a). Boundary-layer behavior on continuous solid surfaces: I. Boundary-layer equations for two-dimensional and axisymmetric flow. AIChE Journal, 7(1), 26–28. https://doi.org/10.1002/aic.690070108
51. Sakiadis, B. C. (1961b). Boundary-layer behavior on continuous solid surfaces: II. The boundary layer on a continuous flat surface. AIChE Journal, 7(2), 221–225. https://doi.org/10.1002/aic.690070211
52. Sanjayanand, E., & Khan, S. K. (2006). On heat and mass transfer in a viscoelastic boundary layer flow over an exponentially stretching sheet. International Journal of Thermal Sciences, 45(8), 819–828. https://doi.org/10.1016/j.ijthermalsci.2005.11.002
53. Shakhaoath Khan, M., Mahmud Alam, M., & Ferdows, M. (2013). Effects of magnetic field on radiative flow of a nanofluid past a stretching sheet. Procedia Engineering, 56, 316–322. https://doi.org/10.1016/j.proeng.2013.03.125
54. Shateyi, S., & Prakash, J. (2014). A new numerical approach for MHD laminar boundary layer flow and heat transfer of nanofluids over a moving surface in the presence of thermal radiation. Boundary Value Problems, 2014, 2. https://doi.org/10.1186/1687-2770-2014-2
55. Shoaib, M., Raja, M. A. Z., Sabir, M. T., Islam, S., Shah, Z., Kumam, P., & Alrabaiah, H. (2020). Numerical investigation for rotating flow of MHD hybrid nanofluid with thermal radiation over a stretching sheet. Scientific Reports, 10, 18533. https://doi.org/10.1038/s41598-020-75254-8
56. Tsegaye, A., Haile, E., Awgichew, G., & Dessie, H. (2025). Effect of nonlinear thermal radiation and Cattaneo–Christov heat and mass fluxes of Williamson hybrid nanofluid over a stretching porous sheet. F1000Research, 14, 210. https://doi.org/10.12688/f1000research.160734.3
57. Uddin, M. J., Khan, W. A., & Ismail, A. I. M. (2012). Scaling group transformation for MHD boundary layer slip flow of a nanofluid over a convectively heated stretching sheet with heat generation. Mathematical Problems in Engineering, 2012, 934964. https://doi.org/10.1155/2012/934964
58. Vishalakshi, A. B., Mahesh, R., Mahabaleshwar, U. S., Rao, A. K., Pérez, L. M., & Laroze, D. (2023). MHD hybrid nanofluid flow over a stretching/shrinking sheet with skin friction: Effects of radiation and mass transpiration. Magnetochemistry, 9(5), 118. https://doi.org/10.3390/magnetochemistry9050118
59. Waqas, H., Farooq, U., Liu, D., Abid, M., Imran, M., & Muhammad, T. (2022). Heat transfer analysis of hybrid nanofluid flow with thermal radiation through a stretching sheet: A comparative study. International Communications in Heat and Mass Transfer, 138, 106303. https://doi.org/10.1016/j.icheatmasstransfer.2022.106303
60. Yashkun, U., Zaimi, K., Abu Bakar, N. A., Ishak, A., & Pop, I. (2020). MHD hybrid nanofluid flow over a permeable stretching/shrinking sheet with thermal radiation effect. International Journal of Numerical Methods for Heat & Fluid Flow, 31(3), 1014–1031. https://doi.org/10.1108/HFF-02-2020-0083